The interplay between surface area and sulfur doping of carbon support on Pt NPs nucleation and growth: A synergistic enhancement of catalytic activity for oxygen reduction

Riccardo Brandiele [a,1], Mattia Parnigotto [a,1], Marco Mazzucato [a], Maria Chiara Dalconi [b], Federica Bertolotti [c], Gian Andrea Rizzi [a], Gregorio Dal Sasso [d], Christian Durante [a,*]

[a] *Department of Chemical Sciences, University of Padova, via Marzolo 1, 35131 Padova, Italy*
[b] *Department of Geoscience University of Padova, via Gradenigo 6, 35131 Padova, Italy*
[c] *Department of Science and High Technology and To.Sca.Lab, University of Insubria, Via Valleggio 11, 22100 Como, Italy*
[d] *Institute of Geosciences and Earth Resources, National Research Council of Italy, Via G. Gradenigo 6, 35131 Padova, Italy*

A R T I C L E   I N F O

A B S T R A C T

Metal–carbon interaction plays a fundamental role in tuning the electrocatalytic behavior of metal nanoparticles (NP). The aim of this study is to emphasize the effective synergy between sulfur doping and the porous structure of the carbon support on the Pt NPs morphology and dimension. Thiophenic-like defects exert a metal-support interaction that affects Pt NPs nucleation and growth and their catalytic activity versus the oxygen reduction reaction (ORR), which makes them promising candidates for the cathode side of PEMFC. Pt NPs defectivity, size, and size dispersion were asserted by using synchrotron wide-angle X-ray total scattering and advanced data analysis. The analyses confirm a mutual correlation between the carbon surface area and the density of sulfur groups with the Pt-specific surface area and with their electrocatalytic properties. The catalytic activity for ORR reaches its peak when a balance is struck between the mesoporosity and the sulfur functionalization of the carbon support.

1. Introduction

Proton exchange membrane fuel cells (PEMFCs) are a well-established electrochemical technology and are commercially available as chemical sources of electricity used in various applications, with a primary focus on hydrogen-powered vehicles [1]. The cathode side of a PEMFC is where a significant portion of polarization loss occurs due to the high activation overpotential of the oxygen reduction reaction (ORR), which is a multistep reaction with a reaction rate several orders of magnitude slower than that of the corresponding H_2 oxidation [2]. Commercial PEMFCs employ platinum as the catalyst for the ORR due to its nearly optimal adsorption energy for the oxygen species involved in this process. However, the use of platinum catalyst significantly contributes to the overall cost of a PEMFC stack. The cost of platinum

catalysts can potentially be reduced to 1% of the total cost of a fuel cell-powered passenger electric vehicle through large-scale production, which typically leads to cost reductions for manufactured systems. However, since the cost of platinum catalysts is primarily a material cost, it does not decrease with the increasing number of fuel cell systems produced per year. Consequently, there are two main approaches to address this challenge: (i) reducing the amount of platinum-based catalyst used, or (ii) completely replacing platinum with a cheaper catalyst, yet equally active and durable [3–5].

The interaction of Pt nanoparticles with carbon supports was found to be a viable way to increase the catalytic activity and stability of the metal [6]. The basis of the metal-carbon interaction is the presence of topological and structural defects as well as heteroatom functional groups such as nitrogen or sulfur, that break the perfect symmetry of a

graphene layer, providing preferential nucleation and growth sites for metal nanoparticles [7,8]. Metal-support interactions can affect the catalytic activity for ORR by influencing the morphology and dimensions of nanoparticles, inducing strain on NPs caused by lattice mismatch, and altering the electronic structure through charge transfer processes [9–13]. Among the different available supports, carbon materials represent a versatile solution for Pt NPs, because they are good electronic conductors, possess good chemical and thermal stability, can be easily functionalized, and their pore structure and surface area can be modified opportunely with the use of templating agents and/or post functionalization [14]. The functionalization of carbon supports involves the introduction of heteroatoms, such as nitrogen, phosphorus, boron, and sulfur, through a process commonly referred to as doping. Many examples of carbon materials have been proposed in the literature (e.g. mesoporous carbon, graphene, and carbon nanohorns or nanotubes), exploiting their properties such as surface area, pore distribution, graphitization, and doping, which can modify NPs formation [15–22]. Among various heteroatoms, sulfur is one of the most fascinating doping elements capable of establishing a distinct metal-support interaction with Pt NPs [19,23]. It was observed that Pt NPs on sulfur doped carbon catalysts exhibited high activity towards the tetraelectronic ORR. The catalytic activity notably increased with the degree of sulfur doping of the carbon support, driving the nucleation and growth of very small (< 2 nm) and dispersed platinum nanoparticles (NPs) [19]. Cheng et al. pointed out that S doping enhances the coordination and electronic structure of Pt species through an already enhanced Pt-N bonding. This induces electron deficiency in adjacent C and N atoms, reinforcing the metal-support interaction [24]. Furthermore, as observed by different authors in the literature, the robust bonding between metal and sulfur at the interface can significantly enhance the adhesion strength between the metal and the sulfur-doped carbon (S-C) support. This, in turn, results in exceptional resistance to sintering even at elevated temperatures as high as 1100 °C [23,25–27]. Choi et al. in collaboration with K. Mayrhofer, also observed that a sulfur-doped carbon structure, specifically a highly curved three-dimensional network of graphene nanoribbons, has the ability to stabilize a relatively high loading of platinum (5 wt%) in the form of atomically dispersed Pt atoms able to catalyze a two-electron ORR pathway producing H_2O_2, rather than the conventional four-electron ORR pathway producing H_2O [28]. The exceptional influence of the sulfur functional group on Pt NPs anchored on the carbon support was observed in several other papers and extended to other reactions of industrial importance including the electro-oxidation of methanol [29], glycerol, and formic acid [30]; the chemoselective hydrogenation of halogenated nitroarenes [31], and even for enhancing the photocatalytic hydrogen evolution reaction at Pt/g-C_3N_4 where the sulfur doping can optimize the band structure and provide a more reactive site for C_3N_4 [32].

Based on the findings from the literature and our own experience in doping mesoporous carbons [20,33–37], modifying their textural properties [14], and investigating how these factors can influence the catalytic properties of platinum nanoparticles [19–21], this study demonstrates, through synchrotron wide-angle X-ray total scattering (WAXTS) experiments coupled to advanced data analysis through the Debye Scattering Equation (DSE) [38,39], the impact of sulfur doping and the micro-mesoporous structure of the carbon support on the formation, growth, surface strain, and ultimately, the catalytic activity of platinum nanoparticles. Pt NPs are grown on sulfur-doped mesoporous carbons (SMC) with different densities of sulfur functional groups (2 < wt% S < 11) and different textural properties induced by steam treatment at high temperatures. DSE method was used for the in-depth characterization of Pt nanoparticles deposited on SMC supports [38, 39], providing a quantitative description of the atomic-scale and nanometer-scale features such as size, shape, lattice strain, and structural defectiveness. Specifically, WAXTS combined with DSE is used to model the influence of sulfur doping and steam treatment on the Pt NPs properties and in turn to assess how they synergistically affect the

performance of Pt NPs versus ORR [40,41],

2. Experimental section

Five different Pt-SMC catalysts were synthesized and characterized along with a Pt/C Tanaka standard (TKK) employed as a reference electrocatalyst. Detailed descriptions of materials and chemicals employed, electrocatalyst synthesis and characterization methods are reported in supporting information. In brief: catalysts were synthesized by depositing Pt nanoparticles onto an SMC carbon support (Figure S1). Before Pt deposition, the carbon support underwent a steam treatment at 850 °C with varying exposure times for each support, from 0 to 60 min, and the corresponding catalysts, after Pt deposition, are named in accordance Pt-SMC_StX (X = 0, 5, 20, 40 and 60 min of steam treatment). The steam treatment results in a gradual reduction of sulfur content, accompanied by an increase in surface area and modulation of the micro-mesopore structure. Therefore, SMC_StX carbon supports differ in terms of a gradual decrease in the density of sulfur functional groups and a gradual increase in surface area and mesopores, which lead to a different nucleation and growth of Pt NPs resulting in Pt NPs of different size and shape. It is worth to stress that this is a multivariable approach and Pt NPs size, sulfur content, and pore size cannot be varied independently but they are the result of the synthesis procedure, for which the variable is the steam treatment.

Pt-SMC_StX catalysts were electrochemically characterized in a three-electrode configuration cell, using a potentiostat/galvanostat Biologic SP-300. The catalysts were tested in a 0.1 M $HClO_4$ solution at 25 °C. A glassy carbon inert electrode (5 mm diameter, geometric surface area 0.196 cm^2) was used as a working electrode. A graphite bar was used as the counter electrode and a reversible hydrogen electrode (RHE) was used as the reference electrode. The catalysts were electrochemically characterized as a thin film, drop-casted on the working electrode. The catalyst ink was formulated for a single drop cast of approximately 12 μL, obtaining a final platinum loading on the electrode of 15 μg cm^{-2}. The ink composition was prepared as follows: 2.2 mg of nanocomposite sample was added to 1.1 mL of H_2O milli-Q grade, 0.1 mL of isopropanol and 1.2 μL of Nafion solution and the resulting suspension was ultrasonicated for 2 h at 25 °C. The catalysts are then carefully drop-casted onto a clean GC surface and allowed to dry under rotation using a rate of 400 rpm at room temperature. The electrolyte was purged with Ar before each measurement, while for the ORR test, the electrolyte was bubbled with high-purity O_2 gas for at least 30 min to ensure O_2 saturation. The catalysts were activated by performing 100 voltammetric cycles at 100 mV s^{-1} between 0.0 V and 1.2 V versus RHE or until stable cyclic voltammograms (CV) were obtained. Catalytic activity versus ORR was evaluated by recording linear sweep voltammograms (LSV) at a scan rate of 20 mV s^{-1} from 1.05 V to 0.05 V and turning back to 1.05 V vs. RHE, in the electrolyte saturated with O_2, using the RDE technique. For the kinetic elaboration, only the return segment is taken into account and subtracted from the background surface oxidation and capacitive processes using the CV recorded in the Ar-saturated solution obtained with the same experimental parameters (i.e., scan speed, rotation rate, potential window).

The electrochemical platinum surface area (EPSA) was calculated from carbon monoxide (CO_{strip}) desorption regions using a charge of 410 μC cm^{-2}. The EPSA for the H_{upd} was evaluated by recording several CV at different scan rates 100 mV s^{-1}, 50 mV s^{-1}, 20 mV s^{-1}, and 5 mV s^{-1} in argon saturated solution. On the other hand, the EPSA from the CO_{strip} is measured at 20 mV s^{-1}. The electrochemical surface area (ECSA) was calculated using the following formula:

$$ECSA = \frac{EPSA}{m_{Pt}} \qquad (1)$$

The kinetic current density j_k was determined using a rotating disk electrode at ω = 1600 rpm. The current density was taken at 0.9 V versus RHE and corrected by mass transfer, according to the

Koutecký–Levich equation

$$j_k = \frac{j_{\text{lim}} \times j_{0.9 \text{Vvs.RHE}}}{j_{\text{lim}} - j_{0.9 \text{Vvs.RHE}}} \tag{2}$$

The mass activity (*MA*) and the specific activity (*SA*), are determined according to the following equations:

$$MA = \frac{j_k}{m_{Pt}} \tag{3}$$

$$SA = \frac{j_k}{EPSA_{CO_{strip}}} \tag{4}$$

Where $EPSA_{CO_{strip}}$ is obtained from the CO stripping measurements. All electrochemical measurements were recorded with the *iR*-drop compensation.

The durability of the catalyst was tested in accelerated stability tests by cycling potentials in the range 0.6÷1.1 V (vs RHE) in 0.1 M HClO$_4$ saturated with O$_2$ at a scan rate of v = 0.5 V s^{-1}; CV at 50 mVs^{-1} and LSV with RDE at 20 mV s^{-1} and 1600 rpm were recorded after every 1000 voltammetric cycles and the results were compared with the standard TKK under the same conditions.

3. Results and discussion

The elemental analysis on Pt-SMC_StX confirmed the different sulfur concentrations depending on the steam treatment time exposition (Table 1) [19,42]. Specifically, the sulfur concentration in Pt-SMC_StX decreases from 10.04 wt% to 1.97 wt% increasing the steam treatment time in SMC from 0 to 60 min (Fig. 1a). Sulfur functional groups are known to produce multiple effects: (i) doping of the carbonaceous material and (ii) a porogenic action [34]. The presence of sulfur in the Pt/C Tanaka standard is not unexpected since even commercially available carbons, such as carbon black and Vulcan XC-72, may contain small amounts of sulfur contamination (less than 1%). ICP-MS revealed a platinum concentration very close to the theoretical value (30%), with a discrepancy against the nominal value of c.a. 3%.

In the prepared samples, it was observed that the surface area increases with longer steam treatment times, as evaluated by using isothermal nitrogen adsorption/desorption analysis at 77 K (Table 1). The results revealed an increase in surface area of almost 500 m^2 g^{-1} going from Pt-SMC_St0 (1103 m^2 g^{-1}) to Pt-SMC_St60 (1674 m^2 g^{-1}) (Fig. 1a). Figure S2a shows the nitrogen adsorption/desorption isotherms for Pt-SMC_StX catalysts. The increase in nitrogen adsorption is due to the increase in mesopore volume, as shown in Table 1. Figure S2b compares the nitrogen adsorption/desorption isotherms of SMC_St5 before and after Pt deposition. It is evident that the presence of Pt nanoparticles only minimally affects the surface area, with a slight reduction in N$_2$ uptake in the mesopore region, while the micropore

region remains mostly unchanged. This indicates preferential nucleation and growth of Pt nanoparticles inside mesopores rather than micropores, with the consequent partial occlusion of the pore network. Figure S3 shows the pore dimensional distribution for the different Pt-SMC_StX catalysts and Pt/C. The micropore surface area remains constant with the increment of the steam time treatment; instead, the mesopore external surface area increases from 957 m^2 g^{-1} to 1478 m^2 g^{-1} passing from the untreated catalyst to Pt-SMC_St60. A similar trend was observed for the volume of micropores and mesopores.

Fig. 1 reports also the TEM images for Pt/C and Pd-SMC_StX catalysts, which show the presence of solid spherical carbon particles, where pores are visible as ordered aligned channels achieving a loosely packed nanostructure. The pores are specular replicas of the mesostructured silica P200 used as templating agents [33]. The carbon particles show a dimension from 150 nm to 300 nm, with a sponge structure that corresponds to the pore channels. Figure S4f shows as an example the SEM images for the carbon SMC_St20. TEM analysis also clearly shows small Pt NPs firmly embedded within the carbon support and inside the pores, whereas some larger nanoparticles randomly form on the surface of the carbon sphere, as confirmed by SEM analysis (Figure S4), in particular for Pt-SMC_St0 and Pt-SMC_St5 (Figure S4a and b). The size distributions of the Pt NPs were obtained by calculating the dimension of ca. 300 randomly distributed NPs on the carbon surface (the TEM imagines for each sample used for the distribution dimension are illustrated in Figure S5). For Pt/C, the mean Pt NP size diameter is centered at ca. 2.7 nm. For the set of Pt NPs on sulfur doped supports, the particle size ranges from 2.2–2.7 nm in the SMC with higher sulfur content and lower surface area (St-0 and St-20) to 3.3–4.7 nm in SMC that has higher surface area and lower sulfur content (St-40 and St-60). The critical size of the clusters (nucleus with the same probability of growth and dissolution), and therefore the particle dimensions, depends on the electronic interaction with the support [40]. This effect on particle size can be attributed, on one hand, to how much high is the density of sulfur functional groups, which facilitate more extensive nucleation of platinum clusters while maintaining smaller nuclei in a stable state. On the other hand, the increase in mesopore size tends to reduce the confinement effect of the pores on the growth of Pt NPs.

Raman investigation of Pt-SMC_StX was performed to obtain information about the structural composition, which could influence the catalytic activity. Figure S6 shows the Raman spectra of the prepared catalysts deconvoluted with four components: D1, D3, D4, and G. Fig. 1b shows the ratio between the area of the band D against the area of the G band for the different catalysts, while Table S1 collects all the deconvolution parameters. All the spectra are normalized to the maximum of the G band and vertically shifted for clarity. The two intense bands observed at approximately 1600 cm^{-1} and 1350 cm^{-1} are the graphitic G band and the defect D1 band, respectively, where the D1 band is related to the disorder and carbon defects [37]. The sulfur-doped

Table 1

Chemical, morphological, and textural properties of platinum on sulfur-doped carbon catalysts.

	S[a]	Pt[b]	S[c]	S$_{\text{micro}}$[d]	S$_{\text{meso}}$[e]	V$_{\text{micro}}$[f]	V$_{\text{meso}}$[g]
	wt%	wt%	m^2 g^{-1}	m^2 g^{-1}	m^2 g^{-1}	m^2 g^{-1}	m^2 g^{-1}
Pt/C	0.75 ± 0.04	49 ± 2	218 ± 11	65 ± 3	153 ± 8	0.030 ± 0.002	0.038 ± 0.002
Pt-SMC_St0	10.04 ± 0.5	27 ± 1	1103 ± 55	146 ± 7	957 ± 48	0.014 ± 0.001	0.86 ± 0.04
Pt-SMC_St5	9.12 ± 0.5	28 ± 1	1278 ± 64	138 ± 7	1140 ± 57	0.045 ± 0.002	0.77 ± 0.04
Pt-SMC_St20	5.34 ± 0.3	26 ± 1	1489 ± 74	94 ± 5	1395 ± 70	0.098 ± 0.005	0.98 ± 0.05
Pt-SMC_St40	3.46 ± 0.1	29 ± 2	1510 ± 76	121 ± 6	1389 ± 69	0.187 ± 0.009	1.38 ± 0.07
Pt-SMC_St60	1.97 ± 0.1	29 ± 2	1674 ± 84	196 ± 10	1478 ± 74	0.37 ± 0.02	2.8 ± 0.1

[a] Elemental weight% from elemental analysis after Pt deposition.
[b] Pt content [wt%] determined by ICP-MS.
[c] BET specific surface area.
[d] Micropore Surface Area.
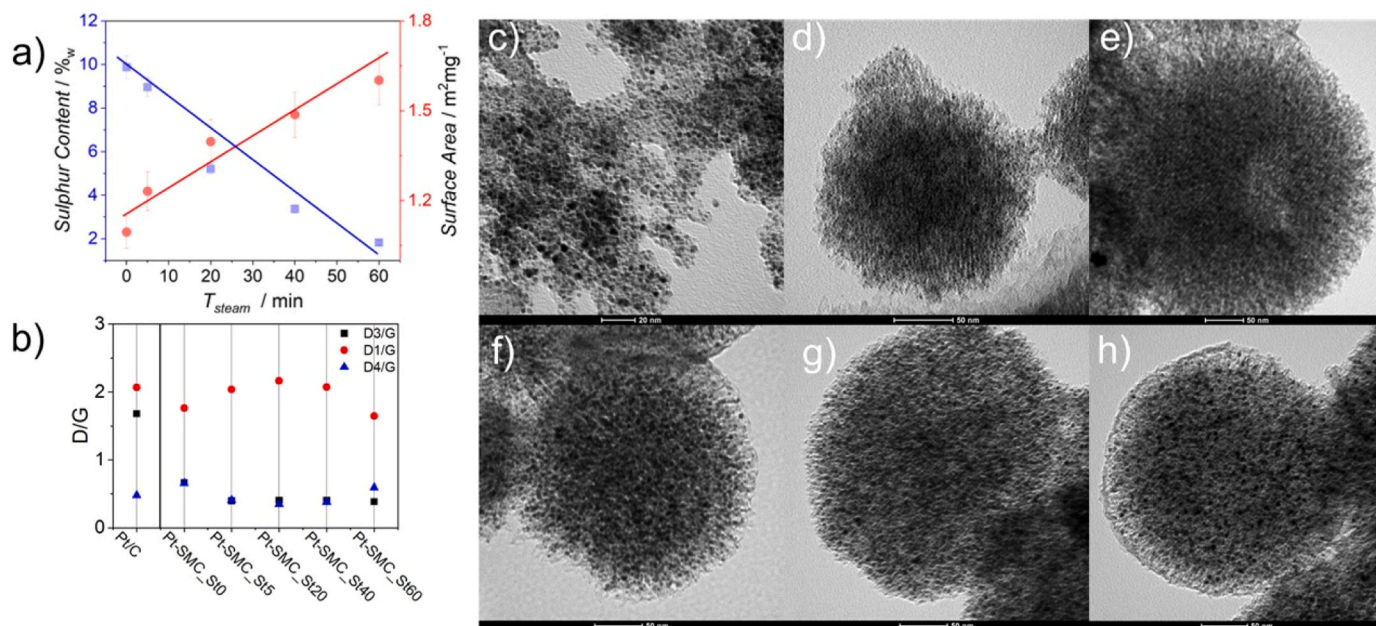[e] Mesopore surface area.
[f] Micropore volume.
[g] Mesopore Volume.

Fig. 1. a) Correlation between the sulfur content, the surface area, and the steam treatment time, b) D_x/G band ratios for the synthesized Pt-SMC_StX. (c-h) TEM images for c) Pt/C; d) Pt-SMC_St0; e) Pt-SMC_St5; f) Pt-SMC_St20; g) Pt-SMC_St40 and h) Pt-SMC_St60. (further TEM images are reported in SI).

carbons show a Raman peak position and a D1/G ratio borderline between Stage 1 and Stage 2 in the Ferrari-Robertson classification [43]. In stage 1, the SMC is made up of graphitic nanocrystals distributed in a graphitic carbon structure, and the cluster dimensions are described by the Tuinstra-Koenig equation, where C (532 nm) = 4.4 [44].

$$\frac{I_D}{I_G} = \frac{C(\lambda)}{L_a} \quad (5)$$

In stage 2, the SMC could be described as graphitic nanocrystals immersed in an amorphous carbon matrix structure. The relationship between I_D/I_G is described by a modified Tuinstra-Koenig equation that binds the intensity ratio in a quadratic dependence with the size of the nanocrystals (L_a), where C' (514 nm) = 0.0055 [35,44].

$$\frac{I_D}{I_G} = C'(\lambda) \times L_a^2 \quad (6)$$

Table S1 and Fig. 1b report the physical properties in terms of the D1/G band ratio, cluster dimension, and crystallite dimension for all Pt-SMC_StX catalysts. The D3 band is attributed to amorphous carbon, and its intensity decreases as the steam treatment increases, eventually reaching a constant D3/G value across all Pt-SMC_StX samples. In fact, the steam treatment is responsible for reacting with the amorphous portion of the carbon support, resulting in the enlargement of mesopores and consequently increasing the proportion of the graphitic component. The D1/G ratio exhibits a maximum value in the Pt-SMC_St20 catalyst and subsequently decreases, indicating the highest level of defectivity in the SMC_St20 support. This observation suggests that in SMC_St20 there is a balance between the density of sulfur functional groups and mesopore content, which are both responsible to afford the maximum defectivity of the catalyst support. Longer steam treatments reduce defectivity by eliminating a portion of the sulfur functional groups and amorphous carbon in general. On the other hand, shorter steam treatments can lead to further oxidation of the carbon support. And last, D4 is commonly assigned to the presence of polyenes or ionic impurities; the D4/G band shows a minimum in Pt-SMC_St20. Pt-SMC_St20 shows the lowest carbon cluster dimension, evaluated according to the Tuinstra-Koenig equation, in stage 1. The crystallite dimension gradually decreases from Pt-SMC_St0 (2.5 nm) passing to a minimum for Pt-SMC_St20 and gradually increases again for Pt-SMC_St60 (2.03 nm),

The XPS survey scans are presented in Figure S7a, while the high-resolution measurements for the Pt 4 f and S 2p signals are reported in Fig. 2 and Figure S7, respectively. The Pt 4 f peak is fitted with 3 components: the first at lower B.E. is assigned to metallic Pt, whereas the less intense components, centered at 72.1 and 73.2 eV, are assigned to oxidized species of Pt(II) and Pt(IV) [45]. It is worth noting that the Pt(0) component increases passing from Pt-SMC-St0 to Pt-SMC-St60 and a corresponding decrease in the amount of Pt(OH)$_2$ and PtO$_2$ is observed (Fig. 2g). Regarding the S 2p signal (Figure S7), although the spectra appear a bit noisy, two distinct contributions can be observed at approximately 164 and 168 eV, which can be respectively assigned to thiophene S (S^{2-}) and to a more oxidized species (-SO$_x$) [46]. On the other hand, in Fig. 2h it is possible to observe a gradual increase in a relative percentage of the thiophene group from Pt-SMC-St20 to Pt-SMC-St60 and a corresponding progressive decrease in the concentration of the -SO$_x$ groups. This clarifies that the steam treatment affects predominantly the oxidized sulfur and therefore it guides not only the S content but also the S chemical form.

4. The DSE analysis of Pt-SMC_StX catalysts

The total scattering approach based on atomistic models, as employed here, is more suited to investigate amorphous and nanocrystalline materials, being able to equally treat both Bragg and diffuse scattering under a unified modelling that can account for size, size distribution, shape and structural defectiveness. In this sense, it is a more powerful, informative, and precise method than the Rietveld analysis. The development of the model for the WAXTS-DSE analysis is reported and comprehensive described in SI, in addition, the results on the structural and microstructural features from the DSE fit for all samples are reported in Table 2. Results are also graphically displayed in Fig. 3 for the sample Pt-SMC_St0, taken as an example, whereas those related to all the other samples are collected in the SI. Table 2 also reports the average estimate lattice strain determined by the refinement of the bulk Pt lattice parameter (a=3.9235 Å). The relative cell contraction is in the range of 0.06÷0.1%, in agreement with other previously published data [47]. Microstrain (ε) has been introduced to account for the angular-dependent peak broadening and the best fit has been obtained for ε in the range of 0.3÷0.4% for all the samples (Fig. 3, a'). In addition,
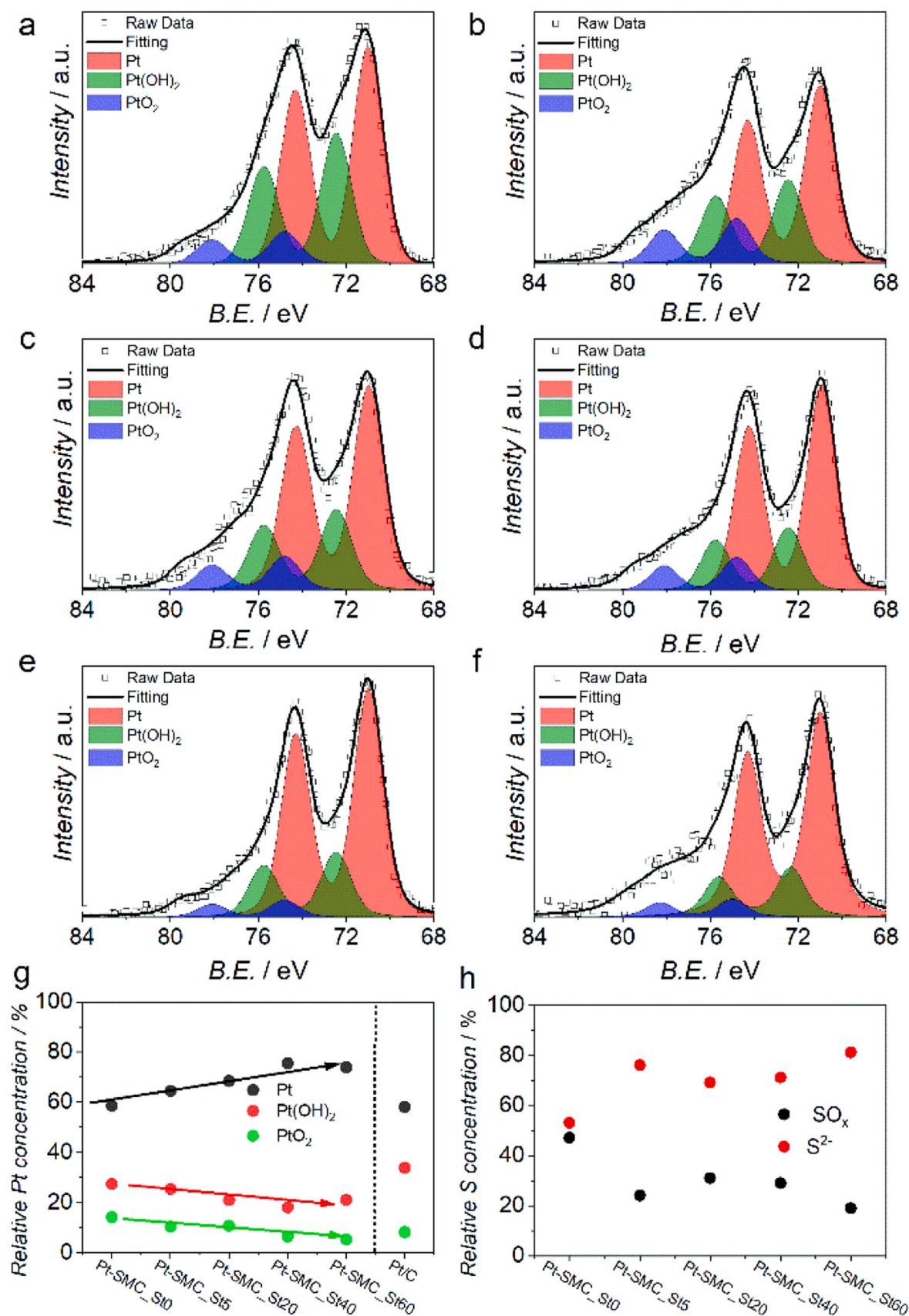
Fig. 2. XPS spectra analysis of Pt 4f components of a) Pt/C; b) Pt-SMC_St0; c) Pt-SMC_St5; d) Pt-SMC_St20; e) Pt-SMC_St40; f) Pt-SMC_St60, g) Relative Pt concentrations in % of Pt-SMC_StX samples compared to those in Pt/C and h) relative S concentrations in % of Pt-SMC_StX samples.

Table 2
Structural and microstructural parameters derived from the best DSE fits for the Pt-SMC_StX samples.

		D_{ab} (nm)	σD_{ab} (nm)	L_c (nm)	σL_c (nm)	c_corr	AR	SSA (m²g⁻¹)	a (Å)	ε	mass fraction	SSA (m²g⁻¹)	GoF
Pt-SMC_St0	P	4.36	2.00	8.49	3.93	0.88	1.9	73.7	3.921	0.004	1	70.8	2.246
Pt-SMC_St5	P	4.91	2.35	15.85	7.22	0.80	3.2	59.3	3.920	0.003	1	59.3	4.354
Pt-SMC_St20	P	2.64	0.93	1.18	0.42	0.93	0.4	175.5	3.919	-	0.98	172.4	1.663
	S	20.00	0.15					14.0	3.923	0.003	0.02		
Pt-SMC_St40	P	2.56	0.91	6.47	1.71	0.96	2.5	102.0	3.921	0.003	0.92	94.7	2.833
	S	20.00	0.15					14.0	3.925	0.003	0.08		
Pt-SMC_St60	P	7.22	4.01	36.75	18.77	0.30	5.1	43.1	3.921	0.004	1	43.1	6.520

Note: 3 samples are modeled through a single population of prismatic (P) Pt NCs, whereas the remaining two are through a double spherical (S)/ prismatic (P) population model. Here are reported the mass-based average size of bivariate (D_{ab}, L_c) and univariate (D_{ab}, in the case of the spherical populations) size distributions, their size dispersions (σD_{ab}, σL_c), the correlation between growth directions in bivariate populations (c-corr), the average aspect ratio AR=L_c/ D_{ab}, the specific surface area SSA for each population and the total SSA weighted for the populations mass fraction for each sample, the average lattice parameter a of the f.c.c. Pt structure, the microstrain parameter ε, and the G.o.F of the DSE fit.
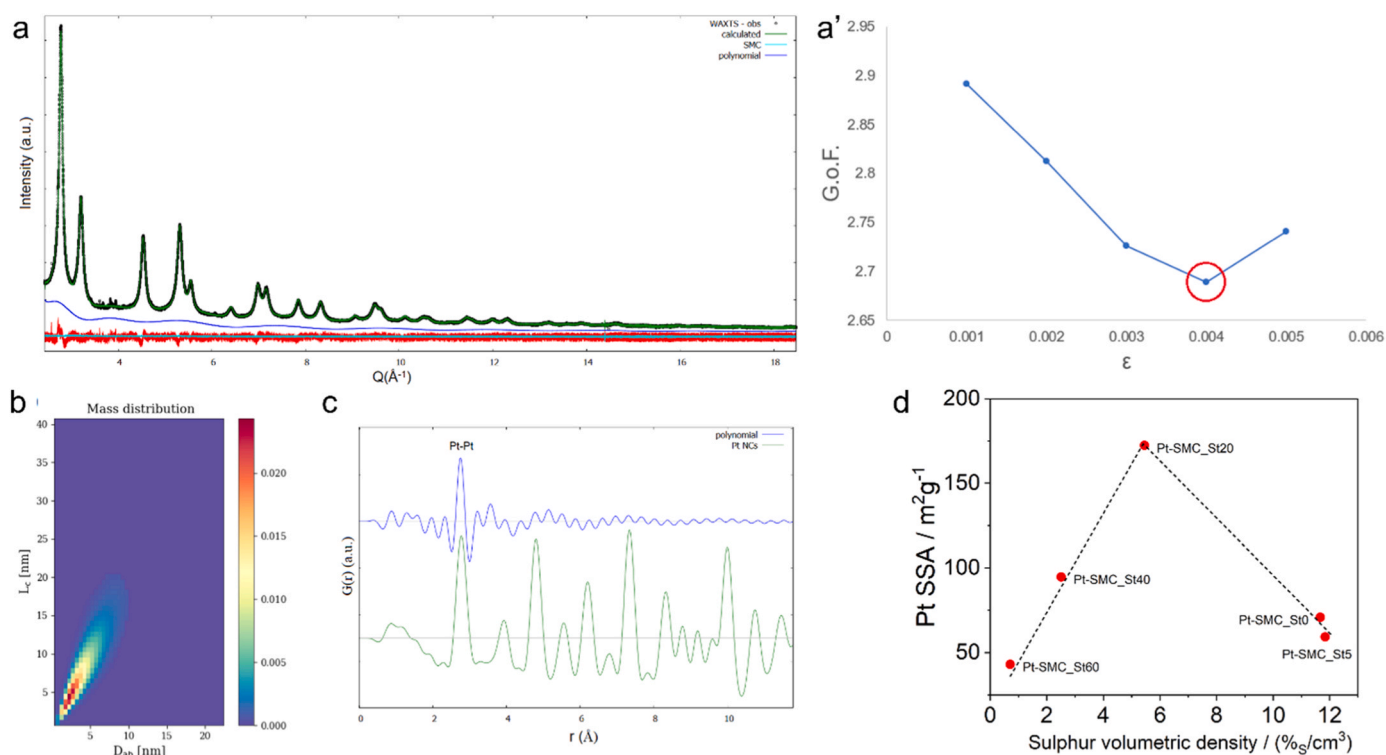

Fig. 3. a) Graphical output of the DSE analysis for the Pt-SMC_St0 sample. WAXTS pattern (black dots) and best fit (green line); the cyan line is the WAXTS pattern of the SMC support used as an additional background phase, the blue line is the polynomial component added to the background function, the red line is the difference between the calculated and experimental patterns. a'), G.o.F. of refined DSE fit vs. microstrain ε, the best fit is obtained for ε = 0.004. b) the 2D map of the bivariate lognormal size distribution of Pt NCs where the mass fraction is given in color code; average D_{ab} and L_c are calculated from projections onto the corresponding axis. c) PDF of the polynomial curve (blue) added to the background function in the DSE analysis and of the DSE simulated scattering pattern of Pt NCs (green). d) volcano-like correlation between Pt SSD, as determined by DSE analysis, with respect to the sulfur percentage normalized by the volume of mesopores.

Table 2 reports the mass-based average size and dispersion for the bivariate prismatic populations of Pt NCs, being parameters more representative for largely polydispersed populations. Instead, the number-based average size and dispersion, which are more comparable with information retrieved from the analysis of TEM images, are reported in Table S2.

The size distribution function is graphically represented by a 2D map of the bivariate lognormal distribution of D_{ab} and L_c for the population of Pt NCs, where the mass fraction is given in color code (Fig. 3b). The average D_{ab} and L_c are calculated from projections onto the corresponding axis. For Pt-SMC_St20 and Pt-SMC_St40 samples, the model included a second population of spherical nanocrystals (NCs), for which the "large" size and low dispersion account for a few large particles occurring in the samples but exceeding the maximum size of the size distribution of prismatic NCs. This choice was adopted to describe the

peculiar shape of the Pt Bragg peaks, for which a sharp contribution was required, as evidenced in the best fit reported in the SI. Given the modest contribution to the whole scattering pattern of these spherical populations, the size and dispersion were kept fixed during the refinement, whereas their relative mass fraction has been scaled within the DSE analysis.

Comparing different samples, the average size, and distributions of the prismatic NCs populations are significantly different among the catalysts, clearly confirming a different nucleation and growth depending on different support, even though each sample is characterized by largely polydispersed populations. The large polydispersity and the correlation angle between the two growing directions account for a significant amount of isotropically shaped NCs (for comparable D_{ab} and L_c), as observed also by TEM images, as well as for markedly elongated NCs with a preferential growth direction along the 111. The average

estimate of the particle elongation is provided by the aspect ratio (L_c/D_{ab}) as reported in Fig. 3b. The anisotropic shape of Pt NCs may be caused by their nucleation and growth within the confined space provided by the pore system of the SMC support. A similar effect was already observed also for Pt NCs deposited on nanoporous silica [47]. For each sample, information from the DSE analysis on the size, morphology, and number- and mass-based size distribution of Pt NCs were also used to calculate the total specific surface area (neglecting aggregation effects between NCs) of the entire population of Pt NCs (Pt SSA, Fig. 3). By examining the size of the prism-shaped particles, it becomes evident from the data presented in Table 2 that the sample Pt-SMC_St20 possesses the smallest dimensions in terms of D_{ab} and L_c, whereas Pt-SMC_St60 possesses the biggest dimensions that align well with TEM analysis. Furthermore, a plot illustrating the Pt SSD, as determined by DSE analysis, in relation to the sulfur volumetric density (i.e., the sulfur percentage normalized by the volume of mesopores), reveals a clear volcano-like correlation (Fig. 3d). This correlation underscores how sulfur functionalization and mesoporous volume exert opposing influences on the dimensions and morphology of the Pt nanoparticles. This leads back to Fig. 1a, where it can be seen that there is a balance between sulfur functionalization and surface area matching the Pt-SMC_ST20 sample. Lastly, the polynomial function, which was added as a model component to the background function to account for a scattering contribution not described by the model (Fig. 3a), shows the

typical broad modulation of an amorphous phase. Interestingly, the polynomial functions among different samples show similar features. The PDF analysis was then applied to these functions to investigate the nature of the scattering component. The G(r) curves Fig. 3c for sample Pt-SMC_St0 (see SI for the other samples) clearly show a peak at 1.76 Å, compatible with the shortest Pt-Pt distance. As for comparison, the G(r) calculated from the DSE simulated pattern of Pt NCs is also reported (Fig. 3c), showing the superimposition of the peak at 1.76 Å, together with peaks related to the longer-range structural correlation of Pt NCs. This provides the possible attribution of the polynomial function, occurring in all the samples, to the scattering contribution of sub-nanometre Pt clusters (being detected only in the first Pt neighbors) or to the occurrence of an amorphous shell covering the Pt nanocrystalline phase.

In conclusion, it can be inferred that the size distributions by TEM and DSE are comparable by considering the number-based distribution, even Pt SSA is determined by mass-based distribution. Both size distributions are provided by the DSE analysis (conversion from one to the other by considering the mass of each particle). Thus, for largely polydisperse population few large particles have a non-negligible weight in a mass-based distribution, moreover, XRD is a mass-sensitive technique. The DSE provides sizes that are averaged over millions of nanocrystals, thus, investigating the whole sample (also inside large clusters not investigated by TEM), results are much more statistically representative
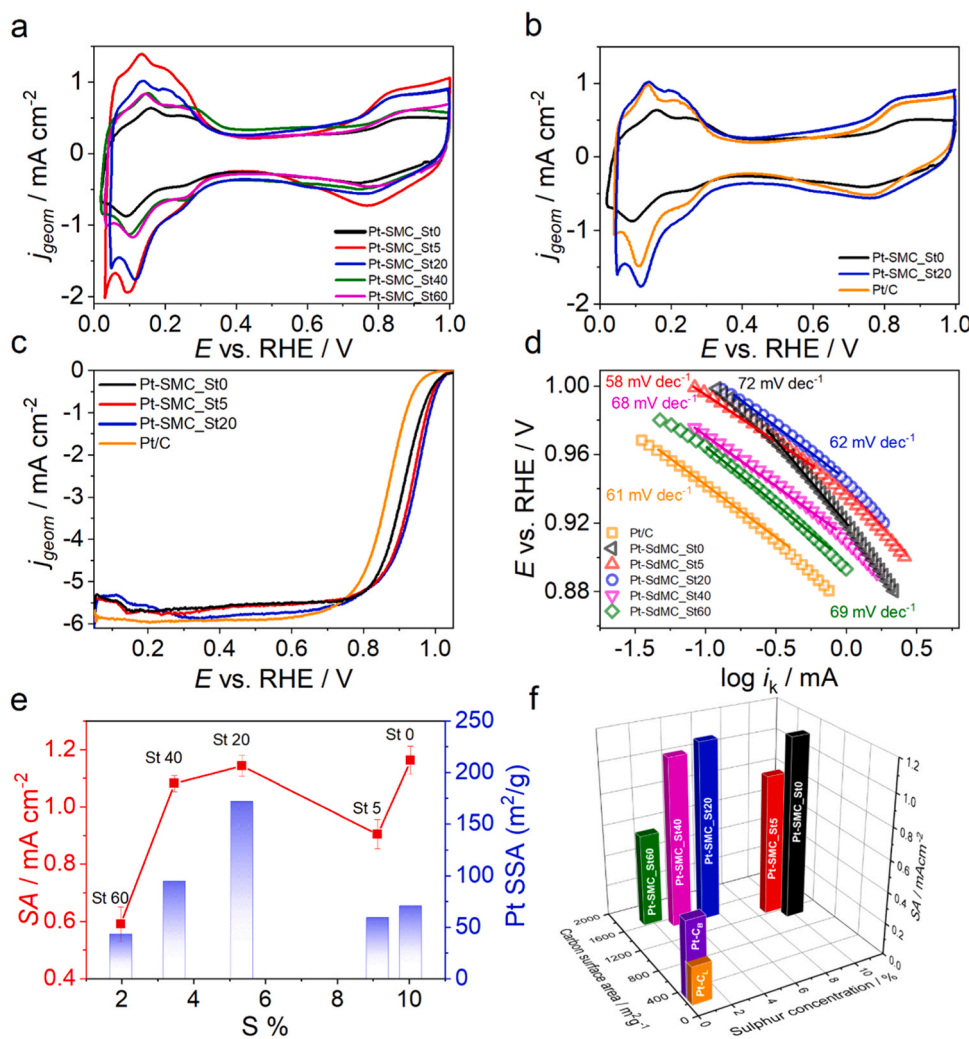

Fig. 4. Electrochemical data in 0.1 M HClO$_4$ for Pt-SMC_StX catalysts. a, b) CVs recorded at 50 mV s^{-1} in Ar purged electrolyte, c) LSVs recorded at 20 mV s^{-1} and 1600 rpm in O$_2$-saturated electrolyte, d) Tafel plot limited to the kinetic region, e) specific activity and Pt SSA as a function of sulfur doping, f) 3D plot, the correlation between the specific activity, the carbon surface area and the sulfur concentration; Pt-C$_B$ is the standard benchmark as reported in literature [48].

than TEM counting, carried out on a limited, albeit substantial, quantity of particles. On the other hand, the quantification of few large particles together with the much more abundant smaller ones provide a clear view on the SSA of the sample that can be correlated to the reactivity, indeed sample inhomogeneity exists, and it must be considered. In this view, TEM counting has the merit of focusing on the small particles much more relevant for the catalytic activity, providing information on the size and aggregation within the sample. Indeed, the DSE is sensitive on nanocrystalline domains (that may or may not coincide with the particle size) but is completely blind on particles aggregation.

5. Electrochemical kinetic analysis

The electrochemical activity was evaluated using cyclic and linear sweep voltammetry techniques in 0.1 M HClO$_4$ electrolyte purged with argon or saturated with oxygen. On the base of DSA analysis, it is reasonable to assert that the catalytic activity is due to the small prismatic-shaped particles rather than to large spherical ones. Fig. 4a shows the CV at 50 mV s^{-1} in an argon-purged solution, for different Pt-SMC_StX catalysts. The CV curves exhibited characteristic regions associated with platinum-based materials: i) PtO$_x$ formation and stripping at a potential greater than 0.65 V vs. RHE, ii) double layer capacitive current between 0.3 V and 0.65 V vs. RHE, and iii) hydrogen adsorption/desorption zone below 0.3 V vs. RHE. In particular, the Pt-SMC_St5 and Pt-SMC_St20 catalysts showed the highest hydrogen adsorption/desorption peaks. Fig. 4b revealed a similar adsorption/desorption region between Pt-SMC_St20 and commercial Pt/C, while Pt-SMC_St60 exhibited a significantly weaker signal. Below 0.2 V versus RHE, the cyclic voltammograms displayed a double peak at 0.095 V vs. RHE and 0.134 V versus RHE, corresponding to hydrogen adsorption at different Pt facets. The EPSA and the relative ECSA are calculated from the CO stripping measurements (Figure S15). Table 3 summarizes the electrochemical results obtained for the Pt-SMC_StX catalysts. Among the synthesized samples, Pt-SMC_St5 and Pt-SMC_St20 exhibited the highest EPSA (1.88 cm^2 and 1.54 cm^2, respectively) and ECSA (64 m^2 g^{-1} and 52 m^2 g^{-1}, respectively). However, these values do not surpass the EPSA and ECSA of standard Pt/C. Despite having a smaller electroactive area, Pt-SMC_St0, Pt-SMC_St5, and Pt-SMC_St20 demonstrated higher activity towards ORR than Pt/C, as clearly evident from Fig. 4c, and outperformed the other samples synthesized with longer steam treatment times (Figure S16). A straightforward approach to demonstrate its superior activity is by comparing the extrapolated half-wave potential ($E_{1/2}$) obtained from the linear sweep voltammograms at RDE in an O$_2$-saturated 0.1 M HClO$_4$ electrolyte (Fig. 4c and Figure S16). The $E_{1/2}$ serves as an indicator to evaluate the catalytic activity of the ORR and varies in descending order of activity: Pt-SMC_St20 > Pt-SMC_St5 > Pt-SMC_St0 > Pt-SMC_St40 > Pt-SMC_St60 > Pt/C. A similar trend was observed when evaluating the mass transfer corrected kinetic current (i_k in Table 3). Pt-SMC_St0 and Pt-SMC_St20 demonstrate also the best performance, in terms of specific activity and mass activity (1.21 mA cm^{-2} / 551 A g^{-1} and 1.14 mA cm^{-2} / 598 A g^{-1}, respectively), followed by Pt-SMC_St5

(0.90 mA cm^{-2} / 577 A g^{-1}). A specific comment is necessary to explain why Pt TKK despite the high active surface area, as matter of fact has lower $E_{1/2}$ or i_k at 0.9 V vs. RHE than Pt-SMC_StX (the same stands for SA and MA, see Table 3). This, apart from a catalytic film preparation procedure that may lead to values somewhat different from the best proposed in the literature (but this would in any case stands for all the samples) [48], is attributable to the higher density of thiophenic groups in Pt-SMC_StX, which can exert an electronic effect as already observed and confirmed in the literature as result of metal support interaction or Pt surface strain [19]. Tafel analysis of the electrochemical data obtained by LSV was evaluated and is reported in Fig. 4d. Typical values of Tafel slope (Ts) for ORR at polycrystalline Pt electrodes in perchloric acid, range between 60 and 120 mV dec^{-1}, depending on factors such as anion adsorption, oxide layer formation, uncompensated resistance, and appropriate selection of boundaries for linear fitting. The similarity in Tafel slopes suggests that the reaction pathway and rate-determining step are comparable between the newly synthesized catalysts and the TKK standard. Pt/C exhibited a Tafel slope of 61 mV dec^{-1} (0.85–0.95 V vs. RHE), consistent with literature reports. Pt-SMC_St20 and Pt-SMC_St5 displayed Tafel slopes of 62 mV dec^{-1} and 58 mV dec^{-1}, respectively, indicating a low oxygen coverage on the Pt surface and faster kinetics for ORR compared to Pt-SMC_St40 and Pt-SMC_St60, which had a lower density of sulfur defects.

By considering the results obtained from elemental analysis for sulfur content, BET for carbon surface area, and synchrotron X-ray total scattering for Pt-specific surface area (Pt SSA) in an aggregated manner, a more comprehensive understanding of the kinetic results can be achieved. Firstly, if we compare the Pt SSA and ECSA (Tables 2 and 3), it seems that the data obtained from DSE analysis overestimated the Pt specific surface area with respect the one determined by CO stripping, but it is worth stressing that the former considers all the platinum present in the sample mass not only the electrochemically active one. Notwithstanding, Fig. 4e demonstrated a good matching between SA and Pt SSA as a function of sulfur content and steam treatment time. This figure highlighted that Pt-SMC_St0 had fewer exposed Pt surface areas compared to Pt-SMC_St20, but in this case metal-support interaction exerts a predominant effect which positively affects the SA as pointed out by Brandiele et al. [19]. The greater Pt SSA in Pt-SMC_St20 was attributed to the optimal sulfur functional group density, which facilitates the nucleation of Pt nanoparticles and, at the same time, the size of mesopores in the carbon support limits the growth of the nucleated Pt nanoparticles. Furthermore, the increased mesoporous structure enhances the platinum-support contact and the exposure to electrolyte. In fact, the other synthesized samples with larger or smaller pore volumes did not prevent agglomeration and excessive growth of Pt NPs, resulting in nonoptimized catalysts in terms of Pt NP morphology. The relationship between surface area (SA) and carbon surface area is visualized in Fig. 4f through a 3D plot. The plot reports also for sake of comparison the Pt/C standard analyzed in this work and the one reported from literature [48]. The plot illustrates the superior activity of Pt-SMC_StX catalysts with respect both the benchmarks. Furthermore, it points out that the decrease in sulfur content resulting from steam treatment is

Table 3
Electrochemical data were obtained from CVs in and LSVs with RDE (20 mV s^{-1} and 1600 rpm) in 0.1 M HClO$_4$ for the different electrode catalysts.

	EPSA[a] cm^2	ECSA CO$_{strip}$ m^2 g^{-1}	$|j_L|$ mA cm^{-2}	$E_{1/2}$[b] V	$\Delta E_{1/2}$ mV	i_k mA	MA A g^{-1}	SA mA cm^{-2}	Ts mV dec^{-1}
Pt/C (TKK)	2.17 ± 0.07	74 ± 2	5.94 ± 0.1	0.867 ± 0.005	0	0.59 ± 0.03	211 ± 10	0.29 ± 0.01	62 ± 3
Pt/C (TKK)[48]		99 ± 5					477 ± 42	0.49 ± 0.05	
Pt-SMC_St0	1.33 ± 0.08	45 ± 3	5.75 ± 0.2	0.906 ± 0.008	39 ± 2	1.62 ± 0.09	551 ± 31	1.21 ± 0.05	72 ± 3
Pt-SMC_St5	1.88 ± 0.06	64 ± 2	5.82 ± 0.09	0.931 ± 0.005	64 ± 3	1.7 ± 0.1	577 ± 48	0.90 ± 0.05	58 ± 9
Pt-SMC_St20	1.54 ± 0.04	52 ± 4	5.6 ± 0.06	0.934 ± 0.008	67 ± 3	1.76 ± 0.09	598 ± 31	1.14 ± 0.04	62 ± 8
Pt-SMC_St40	1.02 ± 0.03	32 ± 1	6 ± 0.06	0.904 ± 0.007	37 ± 2	1.1 ± 0.06	374 ± 20	1.08 ± 0.03	68 ± 3
Pt-SMC_St60	1.36 ± 0.05	46 ± 2	5.49 ± 0.03	0.889 ± 0.005	22 ± 11	0.8 ± 0.1	271 ± 39	0.59 ± 0.06	69 ± 9

[a] values determined by CO stripping.
[b] difference between the E1/2 of the Pt-SMC_Stx compared to the E1/2 of the Pt/C.

offset by an increase in the carbon structure.

Summing up, SMC_StX carbon supports, differing in terms of a gradual decrease of sulfur doping and a gradual increase in surface area and mesopores, guide a different nucleation and growth of Pt NPs resulting in Pt NPs of different size and shape. While in a first approach this might imply a complex matching between morphology/structure and electrocatalytic activity, in reality DSE multiparameter analysis allows a fine rationalization of the different properties of Pt nanoparticles (morphology and the statistic dimension), making catalytic activity easily interpretable based on the morphological/structural properties of the different distributions of Pt NPs.

To investigate catalyst durability, accelerated durability testing (ADT) protocols are commonly employed to simulate the harsh conditions encountered at the cathode of PEMFCs during operation. Pt-SMC_St5, Pt-SMC_St20, and Pt/C materials were electrochemically tested for 10000 CV cycles in an O_2-saturated 0.1 M $HClO_4$ electrolyte. Control CVs at 50 mV s^{-1} and LSV with RDE at 20 mV s^{-1} and 1600 rpm were collected each 1000 cycles. Fig. 5a and b show the LSV with RDE for the pristine material and after 1000, 5000, and 10000 cycles for Pt-SMC_St5 and Pt-SMC_St20, respectively. Fig. 5c and d report the variation of the mass activity and the specific activity during the ADT. Pt/C exhibited a slight increase in specific activity due to the enlargement of Pt nanoparticles to an optimal size for catalyzing the ORR [20,49]. After 10000 cycles, the mass activity decreased by 6%, and at the same time, the specific activity result was almost unchanged. Despite the decrease in kinetic current during the ADT, the SA remains constant because the EPSA decreases with the same trend. The MA for Pt/C TKK decreases by 6%, from 211 A g^{-1} to 195 A g^{-1}. The stability of Pt-SMC_St5 is significantly less than Pt/C after ADT, because $E_{1/2}$ results shifted by 30 mV towards more negative potentials, and the MA and the SA decreased by 55% and 43%, respectively. Pt-SMC_St20 shows MA and SA diminution of 11% and 2%, respectively. The half-wave potential at 10000 cycles results in a decrease of 28 mV compared to the pristine catalyst. Notwithstanding the partial loss of mass activity, Pt-SMC_St20 is much more active and stable than Pt-SMC_St5 and the commercial reference Pt/C TKK.

6. Conclusion

Pt NPs were synthesized by adopting carbon support with a variable density of thiophene-like functional group and increasing mesopore volume and graphitization degree. Synchrotron wide-angle X-ray total scattering experiments coupled with advanced data analysis through the Debye Scattering Equation provided a quantitative description of the atomic- and nanometer-scale features such as size, shape, lattice strain, and structural defectiveness of Pt nanoparticles deposited on SMC_StX supports.

According to DSE analysis, all the Pt NPs show a similar strain notwithstanding the different carbon support, therefore the sole strain cannot account for the different activity observed among the different catalysts. Conversely, the different porous structure and sulfur functional group density were found to deeply affect the shape and dimension of Pt NPs, attesting to a scalable interaction between Pt NPs and the carbon support depending on the sulfur concentration. In fact, the Pt NPs size increases as the thiophenic functional group density decreases or when mesopore size increases, as confirmed also by TEM and BET analysis, respectively. Furthermore, DSE analysis provided information about the Pt specific surface area, which is in good agreement with the one determined by CO electrochemical stripping. In particular, the SSA shows a volcano-like trend, reaching a maximum in the Pt-SMC_St20 sample, which shows the smallest particles thanks to a synergic balance between the maximum extension of the porous structure of the carbon (where the porosity drives the growth of the nanoparticles avoiding an excessive agglomeration) and the maximum allowable sulfur content. The synergic effect of sulfur and textural properties of Pt NPs affect also the activity and stability of Pt NPs finding in Pt-SMC_St20 the best condition for obtaining the most active and at the same time stable catalyst.

Therefore, the study demonstrated that the interaction between Pt NPs and the carbon support could be enhanced by adjusting the sulfur content or optimizing the growth of Pt nanoparticles on the carbon supports by the pore confinement effect. This was demonstrated by the Debye Scattering Equation method, which was fully supported by the typical material analysis techniques (TEM, Raman, BET, CV), but that can represent an innovative and solid protocol of investigation for a
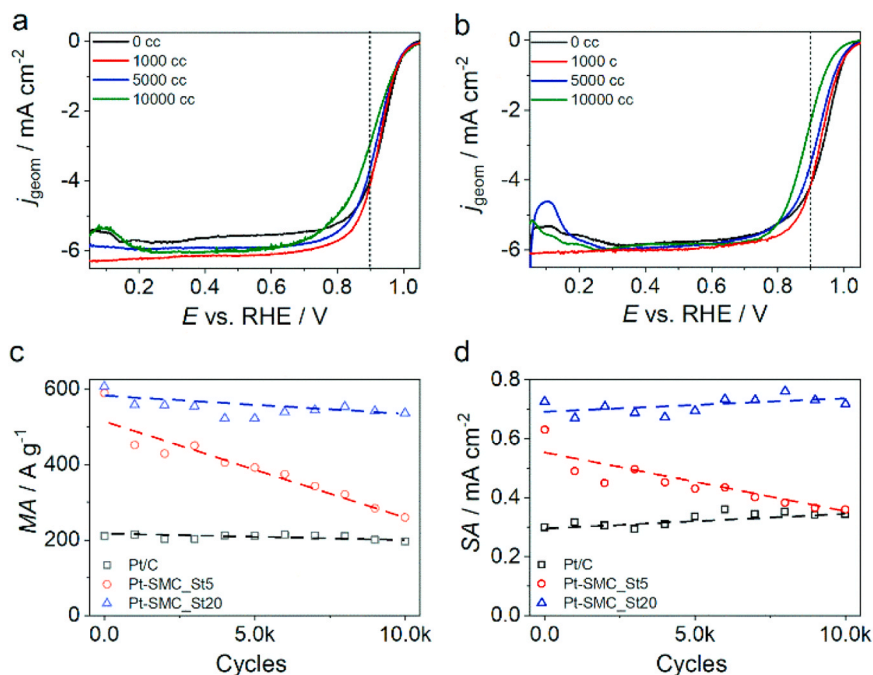

Fig. 5. Accelerated stability tests in O_2-saturated 0.1 M $HClO_4$: 0 cycles black line, 1000 cycles red line, 5000 cycles blue line, and 10000 cycles green line for a) Pt-SMC_St5 and (b) Pt-SMC_St20. (c) Variation of the mass activity and (d) of the specific activity for the tested catalysts.

broader range of nanosized electrocatalysts.

Funding sources

Author contributions

The manuscript was written through contributions of all authors. All authors have given approval to the final version of the manuscript. ‡Riccardo Brandiele and Mattia Parnigotto have contributed equally.

CRediT authorship contribution statement

Brandiele Riccardo: Data curation, Formal analysis. **Durante Christian:** Conceptualization, Funding acquisition, Project administration, Supervision, Writing – original draft, Writing – review & editing. **Dal Sasso Gregorio:** Conceptualization, Data curation, Formal analysis, Writing – original draft, Writing – review & editing. **Rizzi Gian Andrea:** Data curation, Formal analysis. **Bertolotti Federica:** Writing – review & editing. **Dalconi Maria Chiara:** Data curation, Formal analysis. **Mazzucato Marco:** Writing – review & editing. **Parnigotto Mattia:** Data curation, Formal analysis.

Declaration of Competing Interest

The authors declare that they have no known competing financial interests or personal relationships that could have appeared to influence the work reported in this paper.

Data Availability

Data will be made available on request.

Acknowledgment

Supporting information

Experimental details, catalyst synthesis, instruments and methods adopted, Synchrotron Wide Angle X-ray Total Scattering Measurement details, The Debye Scattering Equation (DSE) method details, The Atomic Pair Distribution Function (PDF) method details, supporting tables, Raman and DSE analysis data, supporting figures, Nitrogen adsorption/desorption isotherms, Pore-size distribution, SEM images, Raman spectra, Survey scan and XPS spectra analysis, WAXTS-DSE analysis, CO stripping measurements, ORR performance of catalyst in $HClO_4$ aqueous solution.

Appendix A. Supporting information

Supplementary data associated with this article can be found in the online version at doi:10.1016/j.apcatb.2023.123620.

References

[1] H.A. Gasteiger, N.M. Marković, Just a dream—or future reality? Science 324 (2009) 48–49, https://doi.org/10.1126/science.1172083.

[2] N. Elgrishi, K.J. Rountree, B.D. McCarthy, E.S. Rountree, T.T. Eisenhart, J. L. Dempsey, A practical beginner's guide to cyclic voltammetry, J. Chem. Educ. 95 (2018) 197–206, https://doi.org/10.1021/acs.jchemed.7b00361.

[3] P. Malacrida, H.G. Sanchez Casalongue, F. Masini, S. Kaya, P. Hernández-Fernández, D. Deiana, H. Ogasawara, I.E.L. Stephens, A. Nilsson, I. Chorkendorff, Direct observation of the dealloying process of a platinum-yttrium nanoparticle fuel cell cathode and its oxygenated species during the oxygen reduction reaction, Phys. Chem. Chem. Phys. 17 (2015) 28121–28128, https://doi.org/10.1039/c5cp00283d.

[4] J. Ma, A. Habrioux, Y. Luo, G. Ramos-Sanchez, L. Calvillo, G. Granozzi, P. B. Balbuena, N. Alonso-Vante, Electronic interaction between platinum nanoparticles and nitrogen-doped reduced graphene oxide: effect on the oxygen reduction reaction, J. Mater. Chem. A. 3 (2015) 11891–11904, https://doi.org/10.1039/c5ta01285f.

[5] C. Roy, B.P. Knudsen, C.M. Pedersen, A. Velázquez-Palenzuela, L.H. Christensen, C. D. Damsgaard, I.E.L. Stephens, I. Chorkendorff, Scalable synthesis of carbon-supported platinum-lanthanide and -rare-earth alloys for oxygen reduction, ACS Catal. 8 (2018) 2071–2080, https://doi.org/10.1021/acscatal.7b03972.

[6] C. Durante, Metal–carbon interaction in metal nanoparticles and implication in the electrocatalysis of oxygen reduction, Curr. Opin. Electrochem. 36 (2022), 101119, https://doi.org/10.1016/j.coelec.2022.101119.

[7] Y.-X. Xiao, J. Ying, J.-B. Chen, Y. Dong, X. Yang, G. Tian, J. Wu, C. Janiak, K. I. Ozoemena, X.-Y. Yang, Confined ultrafine Pt in porous carbon fibers and their N-enhanced heavy d-π effect, Chem. Mater. 34 (2022) 3705–3714, https://doi.org/10.1021/acs.chemmater.1c04400.

[8] X. Tong, X. Zhan, Z. Gao, G. Zhang, Y. Xie, J. Tian, H. Ranganathan, D. Li, J. P. Claverie, S. Sun, Effect of the metal–support interaction in platinum anchoring on heteroatom-doped graphene for enhanced oxygen reduction reaction, Chem. Commun. 58 (2022) 11519–11522, https://doi.org/10.1039/D2CC03505G.

[9] A. Anastasopoulos, J.C. Davies, L. Hannah, B.E. Hayden, C.E. Lee, C. Milhano, C. Mormiche, L. Offin, The particle size dependence of the oxygen reduction reaction for carbon-supported platinum and palladium, ChemSusChem 6 (2013) 1973–1982, https://doi.org/10.1002/cssc.201300208.

[10] J. Melke, B. Peter, A. Habereder, J. Ziegler, C. Fasel, A. Nefedov, H. Sezen, C. Wöll, H. Ehrenberg, C. Roth, Metal-support interactions of platinum nanoparticles decorated N-doped carbon nanofibers for the oxygen reduction reaction, ACS Appl. Mater. Interfaces 8 (2016) 82–90, https://doi.org/10.1021/acsami.5b06225.

[11] T. Gao, J. Yang, M. Nishijima, H.A. Miller, F. Vizza, H. Gu, H. Chen, Y. Hu, Z. Jiang, L. Wang, L. Shuai, M. Qiu, C. Lei, A. Zhang, Y. Hou, Q. He, Evidence of the strong metal support interaction in a palladium-ceria hybrid electrocatalyst for enhancement of the hydrogen evolution reaction, J. Electrochem. Soc. 165 (2018) F1147–F1153, https://doi.org/10.1149/2.0351814jes.

[12] R. Brandiele, C. Durante, M. Zerbetto, N. Vicentini, T. Kosmala, D. Badocco, P. Pastore, G.A. Rizzi, A.A. Isse, A. Gennaro, Probing the correlation between Pt-support interaction and oxygen reduction reaction activity in mesoporous carbon materials modified with Pt-N active sites, Electrochim. Acta 277 (2018) 287–300, https://doi.org/10.1016/j.electacta.2018.04.182.

[13] C. Lyu, J. Cheng, Y. Yang, J. Wu, K. Wu, Y. Yang, W.-M. Lau, N. Wang, D. Pang, J. Zheng, Manipulating the interaction of Pt NPs with N-hollow carbon spheres by F-doping for boosting oxygen reduction/methanol oxidation reactions, J. Mater. Chem. A. 11 (2023) 4319–4333, https://doi.org/10.1039/D2TA09416A.

[14] M. Mazzucato, G. Daniel, A. Mehmood, T. Kosmala, G. Granozzi, A. Kucernak, C. Durante, Effects of the induced micro- and meso-porosity on the single site density and turn over frequency of Fe-N-C carbon electrodes for the oxygen reduction reaction, Appl. Catal. B Environ. 291 (2021) 120068–120083, https://doi.org/10.1016/j.apcatb.2021.120068.

[15] J. Biemolt, G. Rothenberg, N. Yan, Understanding the roles of amorphous domains and oxygen-containing groups of nitrogen-doped carbon in oxygen reduction catalysis: toward superior activity, Inorg. Chem. Front. 7 (2019) 177–185, https://doi.org/10.1039/c9qi00983c.

[16] H. Wang, X. Qiu, Z. Peng, W. Wang, J. Wang, T. Zhang, L. Jiang, H. Liu, Cobalt-gluconate-derived high-density cobalt sulfides nanocrystals encapsulated within nitrogen and sulfur dual-doped micro/mesoporous carbon spheres for efficient electrocatalysis of oxygen reduction, J. Colloid Interface Sci. 561 (2020) 829–837, https://doi.org/10.1016/j.jcis.2019.11.065.

[17] O.L. Li, Z. Shi, H. Lee, T. Ishizaki, Enhanced electrocatalytic stability of platinum nanoparticles supported on sulfur-doped carbon using in-situ solution plasma, Sci. Rep. 9 (1) (2019) 10, https://doi.org/10.1038/s41598-019-49194-x.

[18] S. Wang, X. Wang, Q. Deng, Y. Mao, G. Wang, Enhanced oxygen reduction reaction performance of nitrogen-doped carbon nanocages, J. Mater. Sci. Mater. Electron. 30 (2019) 6608–6616, https://doi.org/10.1007/s10854-019-00968-z.

[19] R. Brandiele, M. Zerbetto, M.C. Dalconi, G.A. Rizzi, A.A. Isse, C. Durante, A. Gennaro, Mesoporous carbon with different density of thiophenic-like functional groups and their effect on oxygen reduction, ChemSusChem 12 (2019) 4229–4239, https://doi.org/10.1002/cssc.201901568.

[20] V. Perazzolo, R. Brandiele, C. Durante, M. Zerbetto, V. Causin, G.A. Rizzi, I. Cerri, G. Granozzi, A. Gennaro, Density functional theory (DFT) and experimental evidences of metal–support interaction in platinum nanoparticles supported on nitrogen- and sulfur-doped mesoporous carbons: synthesis, activity, and stability, ACS Catal. 8 (2018) 1122–1137, https://doi.org/10.1021/acscatal.7b03942.

[21] L. Perini, C. Durante, M. Favaro, V. Perazzolo, S. Agnoli, O. Schneider, G. Granozzi, A. Gennaro, Metal–support interaction in platinum and palladium nanoparticles loaded on nitrogen-doped mesoporous carbon for oxygen reduction reaction, ACS Appl. Mater. Interfaces 7 (2015) 1170–1179, https://doi.org/10.1021/am506916y.

[22] L. Perini, C. Durante, M. Favaro, S. Agnoli, G. Granozzi, A. Gennaro, Electrocatalysis at palladium nanoparticles: effect of the support nitrogen doping on the catalytic activation of carbon-halogen bond, Appl. Catal. B Environ. 144 (2014) 300–307, https://doi.org/10.1016/j.apcatb.2013.07.023.

[23] P. Yin, Q. Yan, H. Liang, Strong metal-support interactions through sulfur-anchoring of metal catalysts on carbon supports, Angew. Chem. Int. Ed. (2023), e202302819, https://doi.org/10.1002/anie.202302819.

[24] Y. Chen, X. Zheng, J. Cai, G. Zhao, B. Zhang, Z. Luo, G. Wang, H. Pan, W. Sun, Sulfur Doping Triggering Enhanced Pt–N coordination in graphitic carbon nitride-supported Pt electrocatalysts toward efficient oxygen reduction reaction, ACS Catal. 12 (2022) 7406–7414, https://doi.org/10.1021/ACSCATAL.2C00944.

[25] P. Yin, X. Luo, Y. Ma, S.Q. Chu, S. Chen, X. Zheng, J. Lu, X.J. Wu, H.W. Liang, Sulfur stabilizing metal nanoclusters on carbon at high temperatures, 2021, Nat. Commun. 121 (12) (2021) 1–10, https://doi.org/10.1038/s41467-021-23426-z.

[26] O.L. Li, Z. Shi, H. Lee, T. Ishizaki, EnhanceD Electrocatalytic Stability of Platinum Nanoparticles Supported On Sulfur-doped Carbon Using In-situ Solution Plasma, Sci. Rep. 2019 91. 9 (1) (2019) 10, https://doi.org/10.1038/s41598-019-49194-x.

[27] C.L. Yang, L.N. Wang, P. Yin, J. Liu, M.X. Chen, Q.Q. Yan, Z.S. Wang, S.L. Xu, S. Q. Chu, C. Cui, H. Ju, J. Zhu, Y. Lin, J. Shui, H.W. Liang, Sulfur-anchoring synthesis of platinum intermetallic nanoparticle catalysts for fuel cells, Science 374 (2021) 459–464, https://doi.org/10.1126/SCIENCE.ABJ9980.

[28] C.H. Choi, M. Kim, H.C. Kwon, S.J. Cho, S. Yun, H.T. Kim, K.J.J. Mayrhofer, H. Kim, M. Choi, Tuning selectivity of electrochemical reactions by atomically dispersed platinum catalyst, Nat. Commun. 7 (1) (2016) 9, https://doi.org/10.1038/ncomms10922.

[29] H. Huang, X. Guo, M. Yan, W. Meng, Y. Xue, D. Xiao, Q. Jiang, L. Yang, H. He, Well-dispersive Pt nanoparticles grown on 3D nitrogen- and sulfur-codoped graphene nanoribbon architectures: highly active electrocatalysts for methanol oxidation, Mater. Today Energy 21 (2021), https://doi.org/10.1016/j.mtener.2021.100814.

[30] X. Ning, X. Zhou, J. Luo, L. Ma, X. Xu, L. Zhan, Glycerol and formic acid electro-oxidation over Pt on S-doped carbon nanotubes: Effect of carbon support and synthesis method on the metal-support interaction, Electrochim. Acta 319 (2019) 129–137, https://doi.org/10.1016/j.electacta.2019.06.147.

[31] J. Li, S. Ding, F. Wang, H. Zhao, J. Kou, M. Akram, M. Xu, W. Gao, C. Liu, H. Yang, Z. Dong, Platinum clusters anchored on sulfur-doped ordered mesoporous carbon for chemoselective hydrogenation of halogenated nitroarenes, J. Colloid Interface Sci. 625 (2022) 640–650, https://doi.org/10.1016/j.jcis.2022.06.052.

[32] Z. Li, Y. Yao, X. Gao, H. Bai, X. Meng, Interfacial charge transfer and enhanced photocatalytic mechanisms for Pt nanoparticles loaded onto sulfur-doped g-C$_3$N$_4$ in H$_2$ evolution, Mater. Today Energy 22 (2021), 100881, https://doi.org/10.1016/j.mtener.2021.100881.

[33] V. Perazzolo, C. Durante, R. Pilot, A. Paduano, J. Zheng, G.A. Rizzi, A. Martucci, G. Granozzi, A. Gennaro, Nitrogen and sulfur doped mesoporous carbon as metal-free electrocatalysts for the in situ production of hydrogen peroxide, Carbon 95 (2015) 949–963, https://doi.org/10.1016/j.carbon.2015.09.002.

[34] G. Daniel, M. Mazzucato, R. Brandiele, L. De Lazzari, D. Badocco, P. Pastore, T. Kosmala, G. Granozzi, C. Durante, Sulfur doping versus hierarchical pore structure: the dominating effect on the Fe–N–C site density, activity, and selectivity in oxygen reduction reaction electrocatalysis, ACS Appl. Mater. Interfaces 13 (2021) 42693–42705, https://doi.org/10.1021/acsami.1c09659.

[35] R. Brandiele, L. Picelli, R. Pilot, V. Causin, A. Martucci, G.A. Rizzi, A.A. Isse, C. Durante, A. Gennaro, Nitrogen and sulfur doped mesoporous carbons, prepared from templating silica, as interesting material for supercapacitors, ChemistrySelect 2 (2017) 7082–7090, https://doi.org/10.1002/slct.201701404.

[36] V. Perazzolo, G. Daniel, R. Brandiele, L. Picelli, G.A. Rizzi, A.A. Isse, C. Durante, PEO-b-PS block copolymer templated mesoporous carbons: a comparative study of nitrogen and sulfur doping in the oxygen reduction reaction to hydrogen peroxide, Chem. – A Eur. J. 27 (2021) 1002–1014, https://doi.org/10.1002/chem.202003355.

[37] V. Perazzolo, E. Grądzka, C. Durante, R. Pilot, N. Vicentini, G.A. Rizzi, G. Granozzi, A. Gennaro, Chemical and electrochemical stability of nitrogen and sulphur doped mesoporous carbons, Electrochim. Acta 197 (2016) 251–262, https://doi.org/10.1016/j.electacta.2016.02.025.

[38] P. Debye, Zerstreuung von Röntgenstrahlen, Ann. Phys. 351 (1915) 809–823, https://doi.org/10.1002/andp.19153510606.

[39] A. Cervellino, R. Frison, F. Bertolotti, A. Guagliardi, DEBUSSY 2.0: the new release of a Debye user system for nanocrystalline and/or disordered materials, J. Appl. Crystallogr. 48 (2015) 2026–2032, https://doi.org/10.1107/S1600576715020488.

[40] D. Higgins, M.A. Hoque, M.H. Seo, R. Wang, F. Hassan, J.Y. Choi, M. Pritzker, A. Yu, J. Zhang, Z. Chen, Development and simulation of sulfur-doped graphene supported platinum with exemplary stability and activity towards oxygen reduction, Adv. Funct. Mater. 24 (2014) 4325–4336, https://doi.org/10.1002/adfm.201400161.

[41] K. Kwon, S. Jin, C. Pak, H. Chang, S.H. Joo, H.I. Lee, J.H. Kim, J.M. Kim, Enhancement of electrochemical stability and catalytic activity of Pt nanoparticles via strong metal-support interaction with sulfur-containing ordered mesoporous carbon, Catal. Today 164 (2011) 186–189, https://doi.org/10.1016/j.cattod.2010.10.030.

[42] V. Minkova, S. Marinov, R. Zanzi, E. Björnbom, T. Budinova, M. Stefanova, L. Lakov, Thermochemical treatment of biomass in a flow of steam or in a mixture of steam and carbon dioxide, Fuel Process. Technol. 62 (2000) 45–52, https://doi.org/10.1016/S0378-3820(99)00065-X.

[43] A.C. Ferrari, J. Robertson, Interpretation of Raman spectra of disordered and amorphous carbon, Phys. Rev. B. 61 (2000) 14095–14107, https://doi.org/10.1103/PhysRevB.61.14095.

[44] H. Ning, R.J. Young, D. Wolverson, F. Tanaka, G. Yamamoto, T. Okabe, Investigating nanostructures in carbon fibres using Raman spectroscopy, Carbon 130 (2018) 178–184, https://doi.org/10.1016/j.carbon.2017.12.108.

[45] R. Brandiele, C. Durante, E. Grądzka, G.A. Rizzi, J. Zheng, D. Badocco, P. Centomo, P. Pastore, G. Granozzi, A. Gennaro, One step forward to a scalable synthesis of platinum–yttrium alloy nanoparticles on mesoporous carbon for the oxygen reduction reaction, J. Mater. Chem. A. 4 (2016) 12232–12240, https://doi.org/10.1039/C6TA04498K.

[46] Y. Zan, Z. Zhang, M. Dou, F. Wang, Enhancement mechanism of sulfur dopants on the catalytic activity of N and P co-doped three-dimensional hierarchically porous carbon as a metal-free oxygen reduction electrocatalyst, Catal. Sci. Technol. 9 (2019) 5906–5914, https://doi.org/10.1039/C9CY01387C.

[47] S. Choi, M. Chung, D. Kim, S. Kim, K. Yun, W. Cha, R. Harder, T. Kawaguchi, Y. Liu, A. Ulvestad, H. You, M.K. Song, H. Kim, In situ strain evolution on Pt nanoparticles during hydrogen peroxide decomposition, Nano Lett. 20 (2020) 8541–8548, https://doi.org/10.1021/acs.nanolett.0c03005.

[48] S.S. Kocha, K. Shinozaki, J.W. Zack, D.J. Myers, N.N. Kariuki, T. Nowicki, V. Stamenkovic, Y. Kang, D. Li, D. Papageorgopoulos, Best practices and testing protocols for benchmarking ORR activities of fuel cell electrocatalysts using rotating disk electrode, Electrocatalysis 8 (2017) 366–374, https://doi.org/10.1007/s12678-017-0378-6.

[49] L. Dubau, T. Asset, R. CChattot, B. Bonnaud, V. Vanpeen, J. Netayah, F. Maillard, Tuning the performance and the stability of porous hollow PtNi/C nanostructures for the oxygen reduction reaction, ACS Catal. 5 (2015) 5333–5341, https://doi.org/10.1021/acscatal.5b01248.